

SCIENTIFIC REPORTS



OPEN

The sinking of the El Faro: predicting real world rogue waves during Hurricane Joaquin

Francesco Fedele¹, Claudio Lugni^{2,3}  & Arun Chawla⁴

We present a study on the prediction of rogue waves during the 1-hour sea state of Hurricane Joaquin when the Merchant Vessel El Faro sank east of the Bahamas on October 1, 2015. High-resolution hindcast of hurricane-generated sea states and wave simulations are combined with novel probabilistic models to quantify the likelihood of rogue wave conditions. The data suggests that the El Faro vessel was drifting at an average speed of approximately 2.5 m/s prior to its sinking. As a result, we estimated that the probability that El Faro encounters a rogue wave whose crest height exceeds 14 meters while drifting over a time interval of 10 (50) minutes is $\sim 1/400$ (1/130). The largest simulated wave is generated by the constructive interference of elementary spectral components (linear dispersive focusing) enhanced by bound nonlinearities. Not surprisingly then, its characteristics are quite similar to those displayed by the Andrea, Draupner and Killard rogue waves.

The tragic sinking of the SS El Faro vessel occurred while it was traveling from Florida to Puerto Rico¹. The vessel with a crew of 33 sank about 1140 Hrs UTC on Oct. 1, 2015. As part of their official investigation into the sinking of the El Faro, the National Transportation Safety Board (NTSB) has requested us to carry out an analysis on the occurrence of rogue waves during Hurricane Joaquin around the time and location of the El Faro's sinking². Here, we provide a plain presentation of the main results of our analysis avoiding interpretations, considerations or claims that can be drawn from our studies.

The data suggests that the El Faro vessel was drifting at an average speed of approximately 2.5 m/s prior to its sinking². As a result, El Faro has a higher probability to encounter a rogue wave while drifting over a period of time than that associated with an observer located at a fixed point on the ocean surface. Indeed, the encounter of a rogue wave by a moving vessel is analogous to that of a big wave that a surfer is in search of the surfer's likelihood to encounter a big wave increases if he moves over a large area instead of staying still. Indeed, if he spans a large area the chances to encounter a large wave increase^{3,4}. This is a space-time effect very important for ship navigation and it cannot be overlooked. Such an effect is considered in our rogue wave analysis by way of a new probabilistic model for the exceedance probability, or occurrence frequency of a rogue wave encountered by a vessel along its navigation path^{3,5}. The proposed space-time model provides the basis for the next generation of wave forecast models for a predictive capability of wave extremes and early warnings for shipping companies and others to avoid dangerous areas at risk of rogue waves.

Results

Our rogue wave analysis is focused on the 1-hour sea state of Hurricane Joaquin during which the El Faro vessel sank. This will hereafter be referred to as the El Faro sea state. The wave parameters and statistical models relevant to and required for our analysis are presented in the Methods section.

Metoccean parameters of Hurricane Joaquin in the region of the sinking of El Faro. We use the hindcast directional spectra predicted by WAVEWATCH III and describe the wave characteristics of the sea states generated by Hurricane Joaquin at and around the time and location where the El Faro vessel sank⁶. The top panel on the left of Fig. 1 shows the hourly variation of the significant wave height H_s during the event. The top-right panel displays the time history of the dominant wave period T_p , and the dominant wave direction, the neutral

¹School of Civil & Environmental Engineering, Georgia Institute of Technology, Atlanta, Georgia, 30332, USA.

²CNR-INSEAN & Marine Technology Center - Italian Research Council, Roma, 00128, Italy. ³NTNU-AMOS & Center for Autonomous Marine Operation Systems, Trondheim, 7491, Norway. ⁴National Center for Weather & Climate Prediction, Marine Modelling & Analysis Branch, College Park, 20740, USA. Correspondence and requests for materials should be addressed to F.F. (email: fedele@gatech.edu)

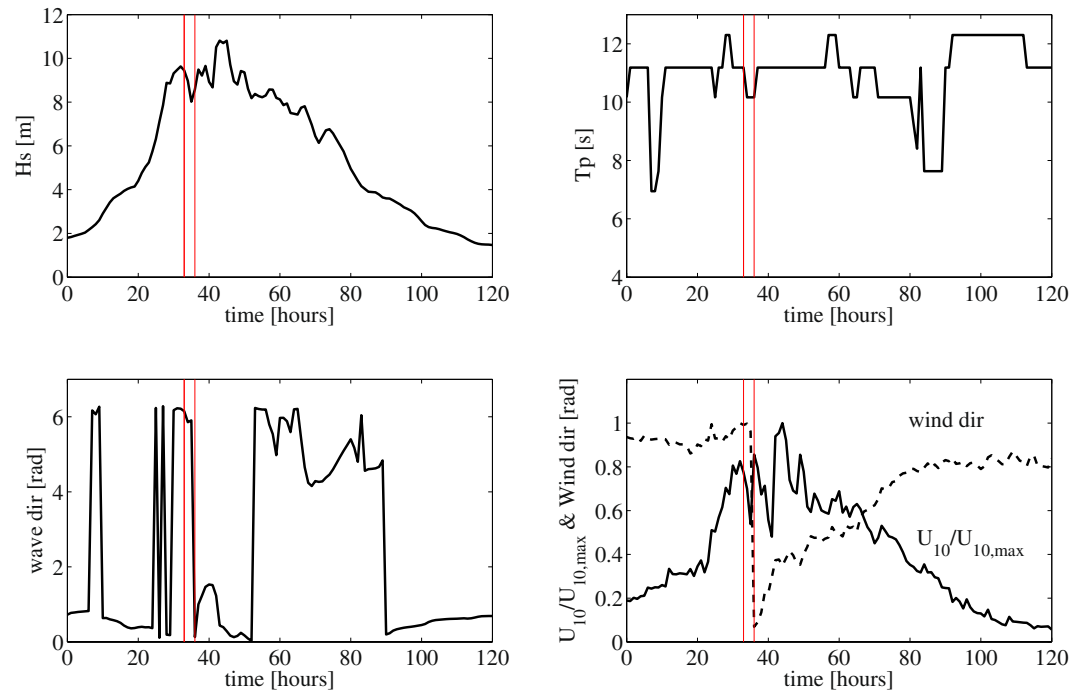


Figure 1. WAVEWATCH III parameters history during Hurricane Joaquin around the location where the El Faro vessel sank. (top-left) Hourly variation of the significant wave height H_s , (top-right) dominant wave period T_p , (bottom-left) dominant wave direction and (bottom-right) normalized $U_{10}/U_{10,max}$ wind speed (solid line) and direction (dashed line). Maximum wind speed $U_{10,max} = 51$ m/s. Red vertical lines delimit the 1-hour interval during which the El Faro vessel sank.

stability 10-m wind speed U_{10} and direction are shown in the bottom-panels, respectively. The red vertical lines delimit the 1-hour interval during which the El Faro vessel sank.

The 1-hour sea state experienced by El Faro at and around the time and location of sinking had a significant wave height of $H_s \approx 9$ m and the maximum wind speed was $U_{10,max} = 51$ m/s. Waves were multidirectional (short-crested) as indicated by the large values of both the spectral bandwidth ν and angular spreading σ_θ as shown in Fig. 2.

In Table 1 we report the metocean parameters of the El Faro sea state in comparison to those of the Draupner, Andrea and Killard rogue sea states⁷. Note that the four sea states have similar metocean characteristics. However, El Faro is a steeper sea state as the mean wavelength L_0 is shorter than those observed in the other three cases.

Statistical properties of Hurricane Joaquin-generated seas. The relative importance of ocean nonlinearities can be measured by integral statistics such as the coefficients of skewness λ_3 and excess kurtosis λ_{40} of the zero-mean surface elevation $\eta(t)$. The skewness is a measure of asymmetry, and it describes the effects of second-order bound nonlinearities on the geometry and statistics of the sea surface with higher sharper crests and shallower more rounded troughs^{8–10}. The excess kurtosis indicates whether the tails of the distribution of surface elevations is heavy- or light-tailed relative to a Gaussian distribution. It comprises a dynamic component λ_{40}^d measuring third-order quasi-resonant wave-wave interactions and a bound contribution λ_{40}^b induced by both second- and third-order bound nonlinearities^{8–13}.

In deep waters, the dynamic kurtosis¹⁴ depends on the Benjamin-Feir index BFI and the parameter R , a dimensionless measure of the multidirectionality of dominant waves^{11, 14, 15}. For unidirectional (1D) waves $R = 0$. The bottom panel of Fig. 2 displays the hourly variations of the directional factor R during Hurricane Joaquin near the location where El Faro sank. Around the peak of the hurricane, the generated sea states are quite multidirectional (short-crested) as $R > 1$. As wave energy also spreads directionally, nonlinear focusing due to modulational instability effects diminishes^{14, 16–18} and becomes essentially insignificant under such realistic oceanic conditions^{7, 14, 19, 20}.

The top panel of Fig. 3 displays the hourly variation of the Tayfun steepness μ (solid line) with associated bounds (dashed lines). The coefficient of excess kurtosis λ_{40} mostly due to bound nonlinearities is shown in the center panel and the associated Λ parameter at the bottom. The red vertical lines delimit the 1-hour interval during which the El Faro vessel sank.

In Table 1 we compare the statistical parameters of the El Faro sea state and the Draupner, Andrea and Killard rogue sea states (from ref. 7). Note that the El Faro sea state has the largest directional spreading. Moreover, for all the four sea states the associated BFI are less than unity and the maximum dynamic excess kurtosis is of $O(10^{-3})$ and thus negligible in comparison to the associated bound component. Thus, third-order quasi-resonant interactions, including NLS-type modulational instabilities play an insignificant role in the formation of large waves^{7, 14}

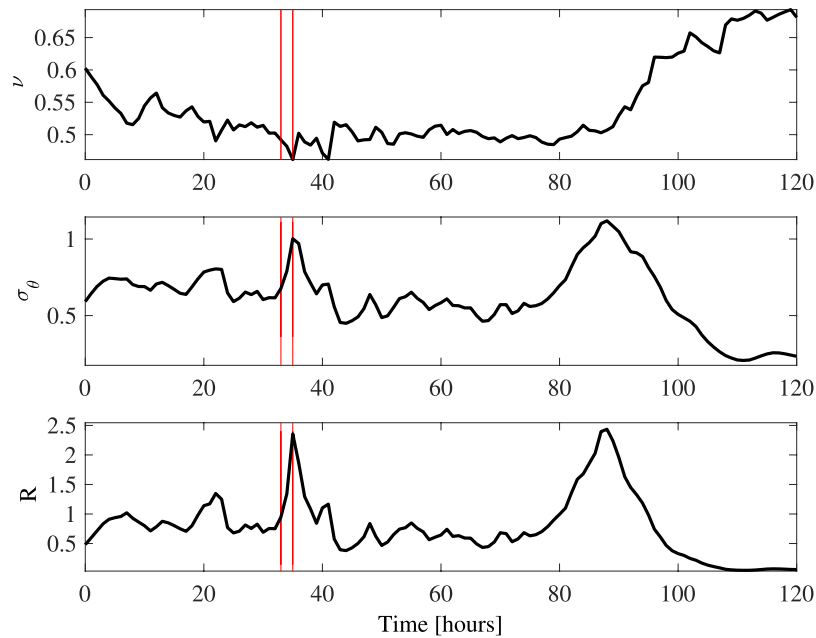


Figure 2. WAVEWATCH III parameters history during Hurricane Joaquin around the location where the El Faro vessel sank. (top) Hourly variation of the spectral bandwidth ν history, (center) directional spreading σ_θ and (bottom) directional factor $R = \frac{1}{2}\sigma_\theta^2/\nu^2$. Red vertical lines delimit the 1-hour interval during which the El Faro vessel sank.

especially as the wave spectrum broadens²¹ in agreement with oceanic observations available so far^{9,22,23}. On the contrary, NLS instabilities have been proven to be effective in the generation of optical rogue waves²⁴.

Higher Order Spectral (HOS) simulations of the El Faro sea state. We have performed Higher-Order pseudo-Spectral (HOS) simulations^{25,26} of the El Faro sea state over an area of $4\text{ km} \times 4\text{ km}$ for a duration of 1 hour (see Methods section for a description of the numerical method). The initial wave field conditions are defined by the WAVEWATCH III hindcast directional spectrum $S(f, \theta)$ around the time and region of the El Faro sinking as shown in Fig. 4. This is the result of a balance of the energy fluxes due to wind input (S_m), exact four-wave resonance nonlinearities (S_{nl}) and dissipation due to wave breaking (S_{ds}). Wind gustiness and currents are not modeled. Our WW3 hindcast indicates that the flux S_m is balanced out by S_{ds} . In particular, around the spectral peak 60% of wind input is lost to dissipation. This offset increases away from the peak. Any wave growth associated with $S_m + S_{ds}$ and S_{nl} is accounted for in the WW3 model. It is the wave growth associated with quasi-resonant and bound harmonics nonlinear effects that is not modeled. In our study, we exploit the HOS wave solver to simulate the El-Faro sea state by accounting for quasi-resonant and bound nonlinearities up to fourth order in wave steepness. An estimate of the most likely rogue wave amplitude is then provided as discussed below. Note that both wind input and wave breaking are somewhat modeled in our HOS simulations as these are initialized with the WW3 spectrum. Clearly, our analysis suggests future studies on the relative importance of possible effects such as wind gustiness²⁷ and wave breaking^{28,29} on the HOS model results.

The wavenumber-frequency spectrum $S(k, \omega)$ estimated from the HOS simulations is shown in Fig. 5. Here, dashed lines indicate the theoretical dispersion curves related to the first-order (1st) free waves as well as the second (2nd) and third-order (3rd) bound harmonic waves. The HOS predictions indicate that second-order nonlinearities are dominant with a weak effect of third-order nonlinear bound interactions, in agreement with recent studies of rogue sea states⁷. It appears that fourth-order effects are insignificant.

The wave skewness and kurtosis rapidly reach a steady state after a few (mean) wave periods as an indication that third-order quasi-resonant wave-wave interactions are negligible in agreement with theoretical predictions¹⁴ and simulations⁷. Note that the theoretical narrowband (NB) predictions slightly overestimate the simulated values for skewness and excess kurtosis (see Table 1). The same trend is also observed in recent studies on rogue waves⁷. This is simply because NB approximations do not account for the directionality and finite spectral bandwidth of the El Faro wave spectrum.

Occurrence frequency of a rogue wave by a fixed observer: the return period of a wave whose crest height exceeds a given threshold. To describe the statistics of rogue waves encountered by an observer at a fixed point of the ocean surface, we consider the conditional return period $N_h(\xi)$ of a wave whose crest height exceeds the threshold $h = \xi H_s$, namely

$$N_h(\xi) = \frac{1}{\Pr[h > \xi H_s]} = \frac{1}{P(\xi)}, \quad (1)$$

	El Faro	Andrea	Draupner	Killard
Significant wave height H_s [m]	9.0	10.0	11.2	11.4
Dominant wave period T_p [s]	10.2	14.3	15.0	17.2
Mean zero-crossing wave period T_0 [s]	9.2	11.1	11.3	13.2
Mean wavelength L_0 [m]	131	190	195	246
Depth d [m], $k_0 d$ with $k_0 = 2\pi/L_0$	4700, 2.63	74, 2.23	70, 2.01	58, 1.36
Spectral bandwidth ν	0.49	0.35	0.36	0.37
Angular spreading σ_θ [rad]	0.79	0.43	0.44	0.39
Parameter $R = \sigma_\theta^2/2\nu^{2.11}$	1.34	0.72	0.75	0.56
Benjamin Feir Index BFI in deep water ^{11,62}	0.36	0.24	0.23	0.18
Tayfun NB skewness $\lambda_{3,NB}$ ^{8-10,61}	0.26	0.159	0.165	0.145
Mean skewness λ_3 from HOS simulations	0.162	0.141	0.146	0.142
Maximum NB dynamic excess kurtosis $\lambda_{40,max}^d$ ¹⁴	10^{-3}	$1.3 \cdot 10^{-3}$	$1.1 \cdot 10^{-3}$	$1.6 \cdot 10^{-3}$
Janssen NB bound excess kurtosis $\lambda_{40,NB}^d$ ^{11,63}	0.049	0.065	0.074	0.076
Mean excess kurtosis λ_{40} from HOS simulations	0.042	0.041	0.032	-0.011
Actual maximum crest height h/H_s	1.68	1.55	1.63	1.62
Actual maximum crest-to-trough (wave) height H/H_s	2.6	2.30	2.15	2.25

Table 1. Wave parameters and various statistics of the simulated El Faro sea state in comparison to the Andrea, Draupner and Killard rogue sea states⁷. We refer to the Methods section for the definitions of wave parameters.

where $P(\xi)$ is the probability or occurrence frequency of a wave crest height exceeding ξH_s as encountered by a fixed observer. In other words, $P(\xi)$ is the probability to randomly pick from a time series observed at a fixed point of the ocean a wave crest that exceeds the threshold ξH_s . Equation (1) also implies that the threshold ξH_s , with $H_s = 4\sigma$, is exceeded on average once every $N_h(\xi)$ waves. For weakly nonlinear random seas, the probability P is hereafter described by the third-order Tayfun-Fedele⁹ (TF), second-order Tayfun⁸ (T), second-order Forristall³⁰ (F) and the linear Rayleigh (R) distributions (see Methods section).

Our statistical analysis of HOS wave data suggests that second-order effects are the dominant factors in shaping the probability structure of the El Faro sea state with a minor contribution of excess kurtosis effects. Such dominance is seen in Fig. 6, where the HOS numerical predictions of the conditional return period $N_h(\xi)$ of a crest exceeding the threshold ξH_s are compared against the theoretical predictions based on the linear Rayleigh (R), second-order Tayfun (T) and third-order (TF) models from Eq. (17). It is noted that the HOS predictions are based on a sample population of 10^6 crests. In particular, $N_h(\xi)$ follows from Eq. (1) as the inverse $1/P(\xi)$ of the empirical probabilities of a crest height exceeding the threshold ξH_s . An excellent agreement is observed between simulations and the third-order TF model up to crest amplitudes $h/H_s \sim 1.5$. For larger amplitudes, the associated confidence bands of the estimated empirical probabilities widen, but TF is still within the bands. Donelan and Magnusson³¹ suggest that the TF model agrees with the Andrea rogue wave measurements up to $h/H_s \sim 1.1$, concluding that TF is not suitable to predict larger rogue crest extremes (see their Fig. 7 in ref. 31). Unfortunately, their analysis is based on a much smaller sampled population of $\sim 10^4$ crest heights and they do not report the confidence bands associated with their probability estimates, nor they provide any parameter values to validate their data analysis. The deviation of their data from the TF model is most likely due to the relatively smaller population of crests observed. Note also that TF slightly exceeds both the T and F models as an indication that second-order effects are dominant, whereas the linear R model underestimates the return periods.

For both third- and fourth-order nonlinearities, the return period N_r of a wave whose crest height exceeds the rogue threshold $1.25H_s \approx 11\text{ m}$ ³² is nearly $N_r \sim 10^4$ for the El Faro sea state and for the simulated Andrea, Draupner and Killard rogue sea states⁷. This is in agreement with oceanic rogue wave measurements²³, which yield roughly the same return period. Similarly, recent measurements off the west coast of Ireland³³ yield $N_r \sim 6 \cdot 10^4$. In contrast, $N_r \sim 3 \cdot 10^5$ in a Gaussian sea.

Note that the largest simulated wave crest height exceeds the threshold $1.6H_s \approx 14\text{ m}$ (see Table 1). This is exceeded on average once every 10^6 waves in a time series extracted at a point in third- and fourth-order seas and extremely rarely in Gaussian seas, i.e. on average once every 10^9 waves. This implies that rogue waves observed at a fixed point of the ocean are likely to be rare occurrences of weakly random seas, or Tayfun sea states³⁴. Our results clearly confirm that rogue wave generation is the result of the constructive interference (focusing) of elementary waves enhanced by bound nonlinearities in agreement with the theory of stochastic wave groups developed by Fedele and Tayfun (2009)¹⁰ as an extension of Boccotti's (2000) theory of quasi-determinism³⁵. Our conclusions are also in agreement with observations^{9,10,12,22}, recent rogue wave analyses^{7,31,36-41} and studies on optical rogue waves caustics analogues⁴².

Time profile of the simulated rogue waves. The wave profile η with the largest wave crest height ($>1.6H_s \approx 14\text{ m}$) observed in the time series of the surface fluctuations extracted at points randomly sparse over the simulated El Faro domain is shown in the left panel of Fig. 7. For comparison, the Draupner, Andrea and Killard rogue wave profiles are also shown⁷. In the same figure, the mean sea level (MSL) below the crests is also shown. The estimation of the MSL follows by low-pass filtering the measured time series of the wave surface with frequency cutoff $f_c \sim f_p/2$, where f_p is the frequency of the spectral peak⁴³. An analysis of the kinematics^{44,45} of the

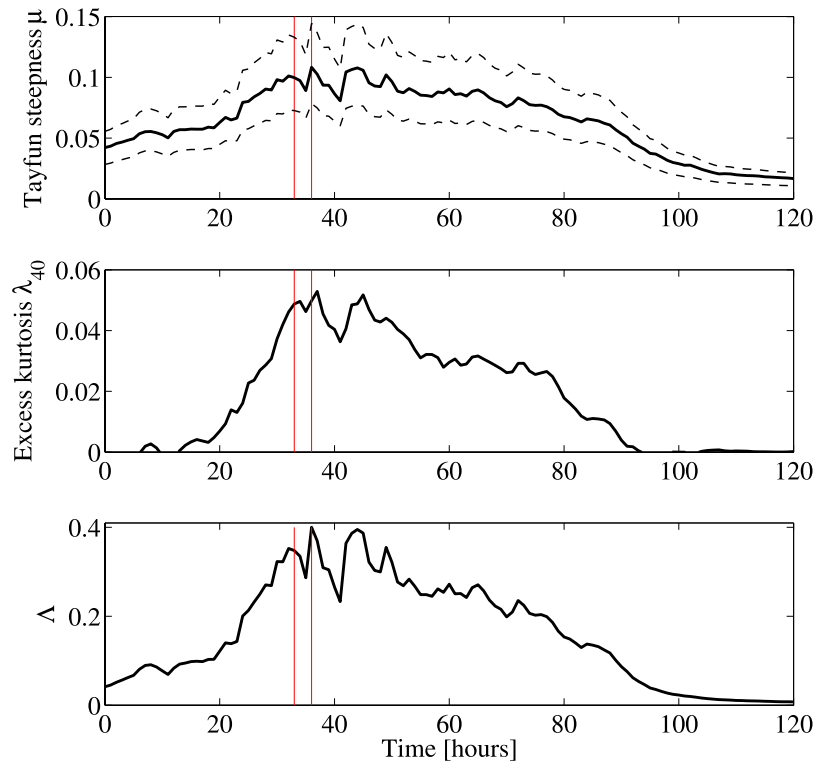


Figure 3. WAVEWATCH III parameters history during Hurricane Joaquin around the location where the El Faro vessel sank. (top) Hourly variation of the Tayfun steepness μ (solid line) with bounds (dashed lines), (center) excess kurtosis λ_{40} and (bottom) nonlinear coefficient $\Lambda \sim 8\lambda_{40}/3$. Red vertical lines delimit the 1-hour interval during which the El Faro vessel sank.

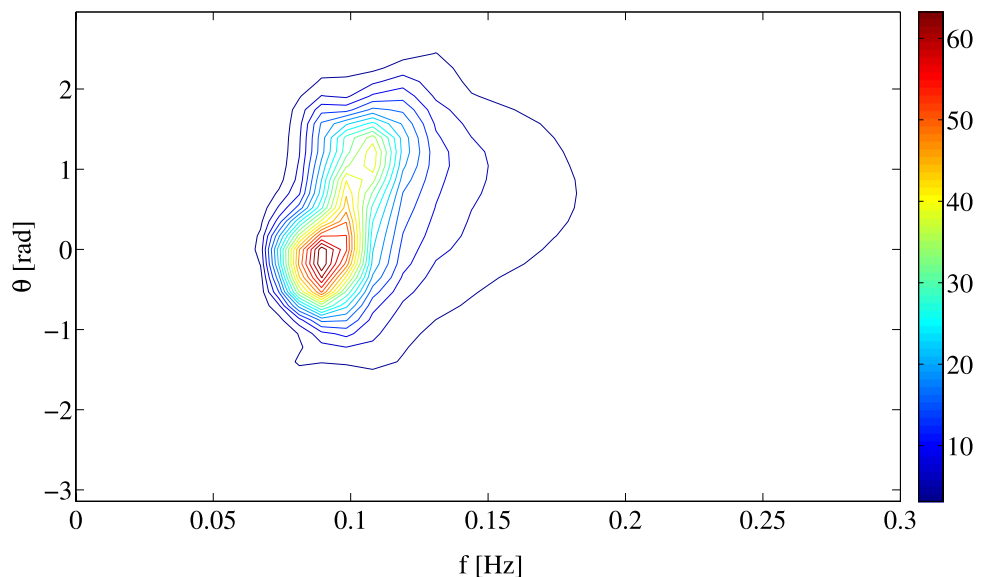


Figure 4. WAVEWATCH III hindcast directional spectrum $S(f, \theta)$ [$m^2/s/rad$] at approximately the time and location of the El-Faro sinking. The zero direction points North and angles increase westward.

simulated rogue waves indicate that such waves were nearly incipient breaking^{28,29,44} suggesting that larger rogue events are less likely to occur^{21,44}. The saturation of the crest height is mainly due to the nonlinear dispersion and it is an energy limiter for rogue waves.

The four wave profiles are very similar suggesting a common generation mechanism of the rogue events. The manner waves are generated by Hurricane Joaquin or the northerly storm of the Draupner, Andrea and Killard sea states, all four waves and their statistics cannot differ in a fundamental way from each other as the

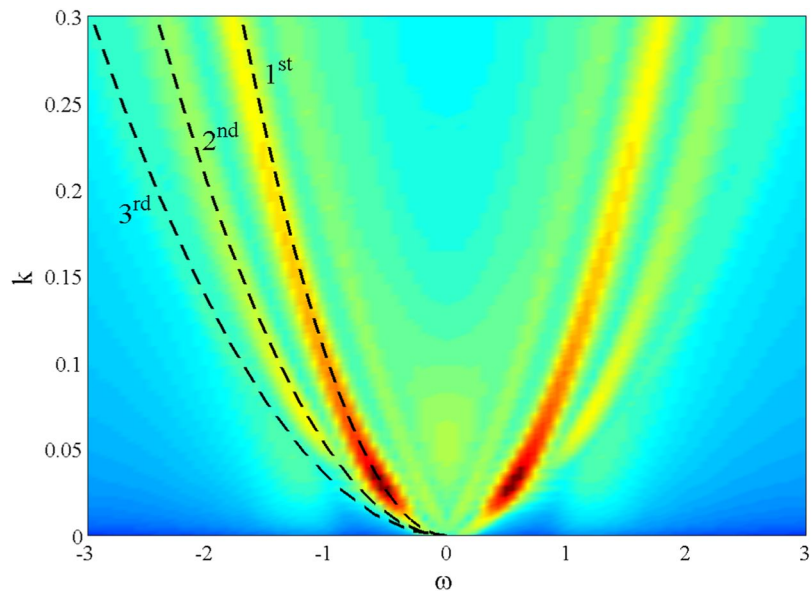


Figure 5. HOS simulations of the El Faro sea state: predicted wavenumber-frequency spectrum $S(k, \omega)$ [$m^2/s/rad$]. Sea state duration of 1 hour over an area of $4\text{ km} \times 4\text{ km}$; the wave field is resolved using 1024×1024 Fourier modes.

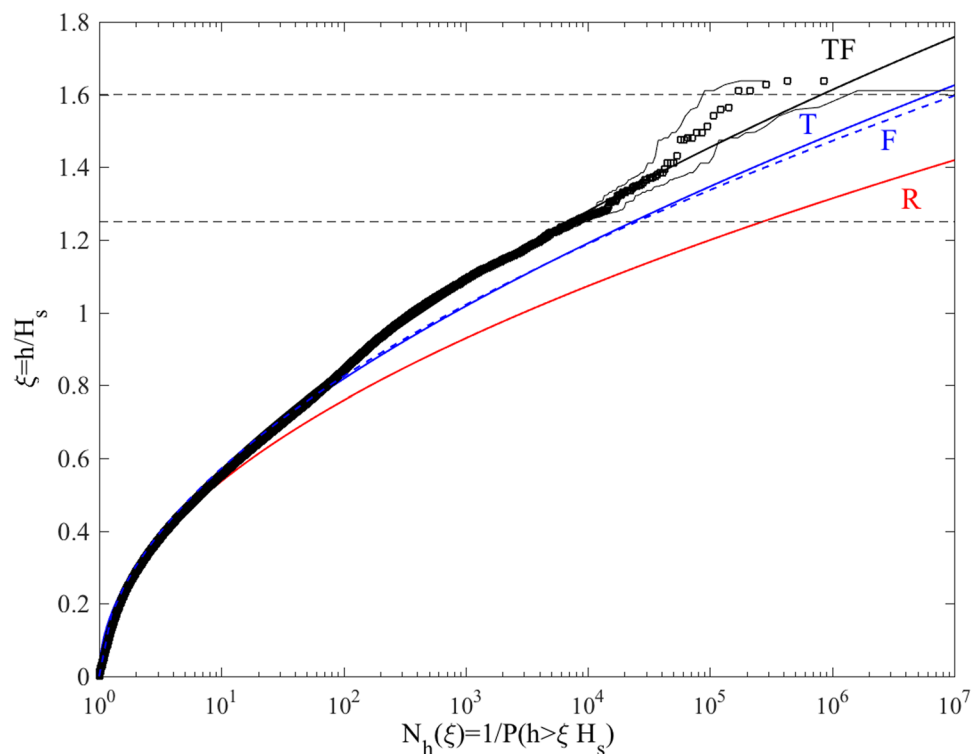


Figure 6. HOS simulations of the El Faro sea state. Crest height scaled by the significant wave height (ξ) versus conditional return period (N_h) for the (left) Andrea, (center) Draupner and (right) Killard rogue sea states: HOS numerical predictions (\square) in comparison with theoretical models: F = Forristall (blue dashed) T = second-order Tayfun (blue solid), TF = third-order (red solid) and R = Rayleigh distributions (red solid). Confidence bands are also shown (light dashes). $N_h(\xi)$ is the inverse of the exceedance probability $P(\xi) = \Pr[h > \xi H_s]$. Horizontal lines denote the rogue threshold $1.25H_s$ ³² and $1.6H_s$.

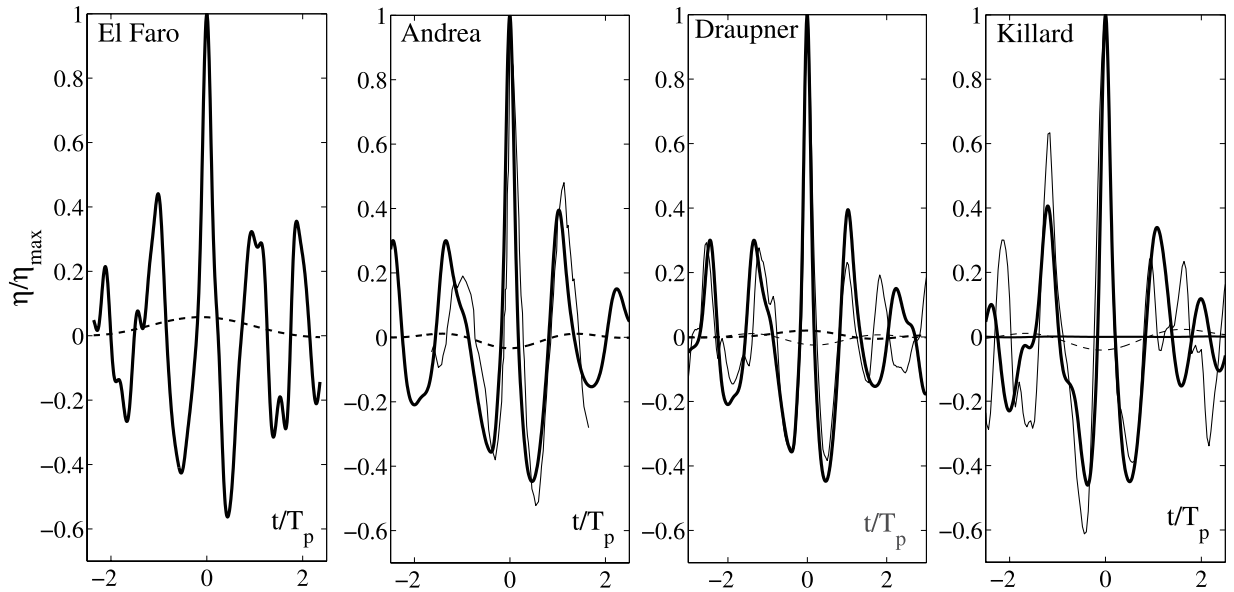


Figure 7. Third-order HOS simulated extreme wave profiles η/η_{max} (solid) and mean sea levels (MSL) (dashed) versus the dimensionless time t/T_p for (from left to right) El Faro, Andrea, Draupner and Killard waves. η_{max} is the maximum crest height given in Table 1. For comparisons, actual measurements (thick solid) and MSLs (tick dashed) are also shown for Andrea, Draupner and Killard. Note that the simulad El-Faro wave is shown in bold. Note that the Killard MSL is insignificant and the Andrea MSL is not available. T_p is the dominant wave period (see Methods section for definitions).

spectral shape of the four sea states is similar showing only some variations in terms of directionality or frequency characteristics.

Further, we observe a set-up below the simulated El Faro rogue wave, most likely due to the multidirectionality of the sea state. A set-up is also observed for the actual Draupner rogue wave. Indeed, recent studies showed that Draupner occurred in a crossing sea consisting of swell waves propagating at approximately 80 degrees to the wind sea^{46,47}. This would explain the set-up observed under the large wave⁴³ instead of the second-order set-down normally expected⁴⁸.

Space-time statistics of the sea state encountered by El Faro before sinking. The largest crest height of a wave observed in time at a given point of the ocean represents a maximum observed at that point. Clearly, the maximum wave surface height observed over a given area during a time interval, i.e. space-time extreme, is much larger than that observed at a given point. Indeed, in relatively short-crested directional seas such as those generated by hurricanes, it is very unlikely that an observed large crest at a given point in time actually coincides with the largest crest of a group of waves propagating in space-time. In contrast, in accord with Boccotti’s (2000) QD theory³⁵, it is most likely that the sea surface was in fact much higher somewhere near the measurement point.

Space-time wave extremes can be modeled stochastically^{3,4} drawing on the theory of Euler Characteristics of random fields^{49–51} and nonlinear wave statistics¹⁴. In the following, we present the Fedele’s Space-Time (FST) stochastic model for the prediction of space-time extremes³ that accounts for both second and third-order nonlinearities⁵. Fedele’s work^{3,5} considers a 3-D non-Gaussian field $\eta(x, y, t)$ in space-time over an area A for a time period of D (see Fig. 8). The area cannot be too large since the wave field may not be homogeneous. The duration should be short so that spectral changes occurring in time are not significant and the sea state can be assumed as stationary. Then, the third-order nonlinear probability $P_{FST}^{(nl)}(\xi; A, D)$ that the maximum surface elevation η_{max} over the area A and during the time interval D exceeds the generic threshold ξH_s is described by⁵

$$P_{FST}^{(nl)}(\xi; A, D) = P_{ST}(\xi_0; A, D)(1 + A\xi_0^2(4\xi_0^2 - 1)), \tag{2}$$

where

$$P_{ST}(\xi; A, D) = \Pr\{\eta_{max} > \xi H_s\} = (16M_3\xi^2 + 4M_2\xi + M_1)P_R(\xi) \tag{3}$$

denotes the Gaussian probability of exceedance, and $P_R(\xi)$ is the Rayleigh exceedance probability of Eq. (19).

Here, M_1 and M_2 are the average number of 1-D and 2-D waves that can occur on the edges and boundaries of the volume Ω , and M_3 is the average number of 3-D waves that can occur within the volume³. These all depend on the directional wave spectrum and its spectral moments m_{ijk} defined in the Methods section.

The amplitude ξ relates to ξ_0 via the Tayfun (1980) quadratic equation⁸

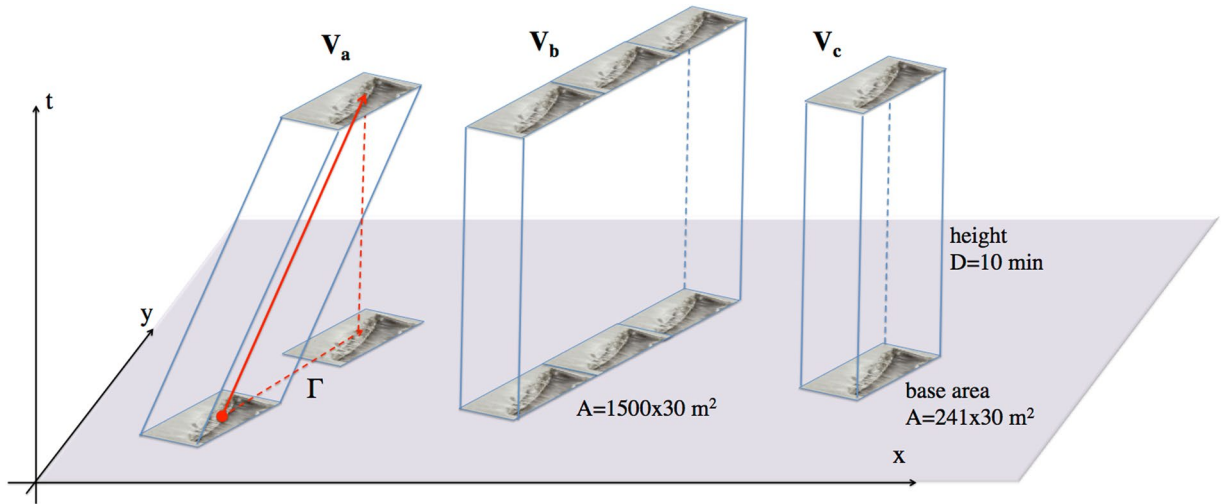


Figure 8. (Left) the space-time (xyt) volume spanned by the El Faro vessel (base area $A = 241 \times 30 \text{ m}^2$) while drifting at the speed of 2.5 m/s over a time interval of $D = 10$ minutes along the path Γ is that of the slanted parallelepiped V_a ; (center) the drifting vessel covers the strip area ($1500 \times 30 \text{ m}^2$) in the 10-minute interval and the associated space-time volume is that of the parallelepiped V_b ; (right) if the vessel would be anchored at a location for the same duration, it would span instead the spacetime volume of the straight parallelepiped V_c . The solid red arrowed line denotes the space-time path of El Faro while drifting along the path Γ . The vertical axis is time (t) and the other two axes refer to the space dimensions (x) and (y) respectively.

$$\xi = \xi_0 + 2\mu\xi_0^2. \tag{4}$$

Given the probability structure of the wave surface defined by Eq. (2), the nonlinear mean maximum surface or crest height $\bar{h}_{\text{FST}} = \xi_{\text{FST}} H_s$ attained over the area A during a time interval D is given, according to Gumbel (1958), by^{4,5}

$$\xi_{\text{FST}} = \bar{h}_{\text{FST}}/H_s = \xi_m + 2\mu\xi_m^2 + \frac{\gamma_e(1 + 4\mu\xi_m)}{16\xi_m - \frac{32M_3\xi_m + 4M_2}{16M_3\xi_m^2 + 4M_2\xi_m + M_1} - \Lambda \frac{2\xi_m(8\xi_m^2 - 1)}{1 + \Lambda\xi_m^2(4\xi_m^2 - 1)}}, \tag{5}$$

where the most probable surface elevation value ξ_m satisfies $P_{\text{ST}}(\xi_m; A, D) = 1$ (see Eq. (2)) and the Euler-Mascheroni constant $\gamma_e \approx 0.577$.

The nonlinear mean maximum surface or crest height h_T expected at a point during the time interval D follows from Eq. (5) by setting $M_2 = M_3 = 0$ and $M_1 = N_D$, where $N_D = D/\bar{T}$ denotes the number of waves occurring during D , and \bar{T} is the mean up-crossing period (see Methods section). The second-order form of the FST model ($\Lambda = 0$) has been implemented in WAVEWATCH III⁵². The linear limit follows from Eq. (5) by setting $\mu = 0$ and $\Lambda = 0$.

The statistical interpretations of the probability $P_{\text{FST}}^{(nl)}(\xi; A, D)$ and associated space-time average maximum \bar{h}_{ST} are as follows. Consider an ensemble of N realizations of a stationary and homogeneous sea state of duration D , each of which has similar statistical structure to the El Faro wave field. On this basis, there would be N samples, say $(\eta_{\text{max}}^{(1)}, \dots, \eta_{\text{max}}^{(N)})$ of the maximum surface height η_{max} observed within the area A during the time interval D . Then, all the maximum surface heights in the ensemble will exceed the threshold \bar{h}_{FST} . Clearly, the maximum surface height exceeds by far such average. Indeed, only in a few number of realizations $N \cdot P_{\text{FST}}^{(nl)}(\xi; A, D)$ out of the ensemble of N sea states, the maximum surface height exceeds a threshold $\xi H_s \gg \bar{h}_{\text{FST}}$ much larger than the expected value. To characterize such rare occurrences in third-order nonlinear random seas one can consider the threshold $h_q = \xi_q H_s$ exceeded with probability q by the maximum surface height η_{max} over an area A during a sea state of duration D . This satisfies

$$P_{\text{FST}}^{(nl)}(\xi_q; A, D) = q. \tag{6}$$

The statistical interpretation of h_q is as follows: the maximum surface height η_{max} observed within the area A during D exceeds the threshold h_q only in qN realizations of the above mentioned ensemble of N sea states.

Note that for large areas, i.e. $\ell \gg L_0$, our FST model as any other similar models available in literature^{47, 53–56} will overestimate the maximum surface height over an area and time interval because they all rely on Gaussianity. This implies that there are no physical limits on the values that the surface height can attain as the Gaussian model does not account for the saturation induced by the nonlinear dispersion²¹ of ocean waves or wave breaking. Thus,

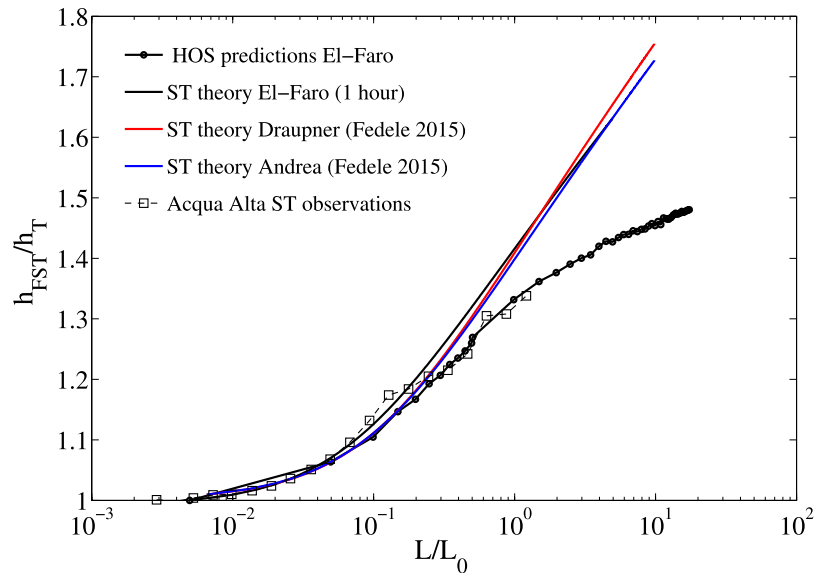


Figure 9. Space-time extremes: theoretical FST ratios $\bar{h}_{\text{FST}}/\bar{h}_T$ as a function of the area width ℓ/L_0 for El Faro (black), Draupner (red) and Andrea (blue) sea states, where \bar{h}_{FST} is the mean maximum surface height expected over the area ℓ^2 during a sea state of duration $D=1$ hours and \bar{h}_T is the mean maximum surface height expected at a point. For comparisons, the empirical FST ratio from the El Faro HOS simulations (dashed line with circles) together with the experimental observations at the Acqua Alta tower (squares) are also shown⁴. L_0 is the mean wavelength.

the larger the area A or the time interval D , the greater the number of waves sampled in space-time, and unrealistically large amplitudes are likely to be sampled in a Gaussian or weakly nonlinear Gaussian sea.

This point is elaborated further and demonstrated explicitly by way of the results displayed in Fig. 9. Here, the theoretical (FST) ratio $\bar{h}_{\text{FST}}/\bar{h}_T$ as a function of the area width ℓ/L_0 is shown for the El Faro, Draupner and Andrea sea states respectively. The FST ratios for Draupner and Andrea are estimated using the European Reanalysis (ERA)-interim data⁵. For comparisons, the empirical ST ratio from the El Faro HOS simulations together with the experimental observations at the Acqua Alta tower⁴ are also shown. Recall that \bar{h}_{FST} is the mean maximum surface height expected over the area ℓ^2 during a sea state of duration $D=1$ hour and \bar{h}_T is the mean maximum surface height expected at a point. Clearly, the theoretical FST ratio for El Faro fairly agrees with the HOS simulations for small areas ($\ell \leq L_0$), whereas it yields overestimation over larger areas. We argue that the saturation of the HOS FST ratio over larger areas is an effect of the nonlinear dispersion which is effective in limiting the wave growth as a precursor to breaking^{21, 44}.

Note that the FST ratios for all the three sea states are nearly the same for $\ell \leq L_0$. These results are very encouraging as they suggest possible statistical similarities and universal laws for space-time extremes in wind sea states⁵. Moreover, for $\ell \sim L_0$ the mean wave surface maximum expected over the area is 1.35 times larger than that expected at a point in agreement with Acqua Alta sea observations⁴.

The occurrence frequency of a rogue wave by the El Faro vessel. The data suggests that the El Faro vessel was drifting at an average speed of approximately 2.5 m/s prior to its sinking. This is considered in our analysis as follows. First, define the two events R = “El Faro encounters a rogue wave along its navigation route” and S = “El Faro sinks”. We know that the event S happened. As a result, one should consider the conditional probability

$$\Pr[R|S] = \frac{\Pr[S|R] \cdot \Pr[R]}{\Pr[S]} \quad (7)$$

Here, $\Pr[S]$ is the unconditional probability of the event that El Faro sinks. This could be estimated from worldwide statistics of sunk vessels with characteristics similar to El Faro. $\Pr[S|R]$ is the conditional probability that El Faro sinks given that the vessel encountered a rogue wave. This probability can be estimated by Monte Carlo simulations of the nonlinear interaction of the vessel with the rogue wave field.

Our rogue wave analysis provides an estimate of the unconditional probability $\Pr[R]$ that El Faro encounters a rogue wave along its navigation or drifting route by means of the exceedance probability, or occurrence frequency $P_e(h)$. This is the probability that a vessel along its navigation path encounters a rogue wave whose crest height exceeds a given threshold h . The encounter of a rogue wave by a moving vessel is analogous to that of a big wave that a surfer is in search of. His likelihood to encounter a big wave increases if he moves around a large area instead of staying still. This is a space-time effect which is very important for ship navigation and must be accounted for^{3, 57–60}.

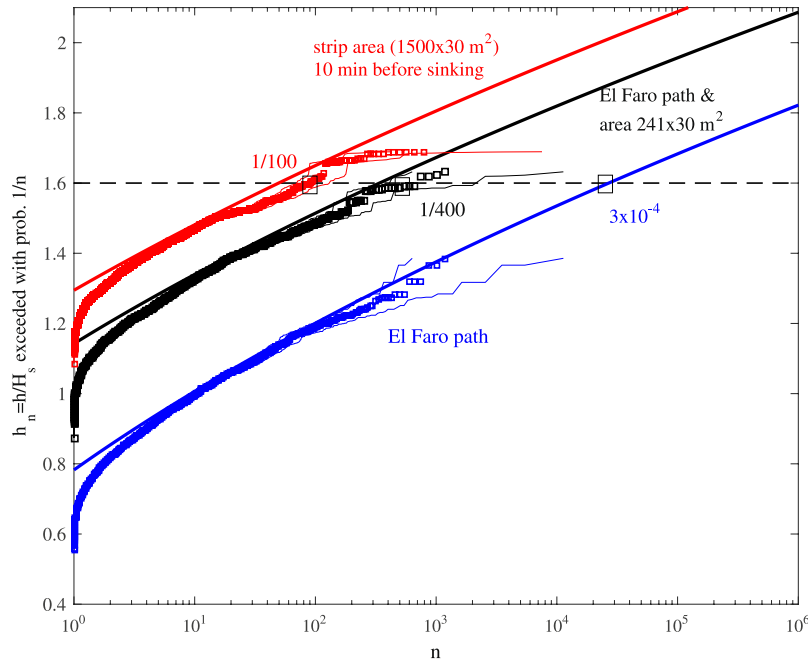


Figure 10. HOS (squares) and theoretical (solid lines) predictions for the normalized nonlinear threshold h_n/H_s exceeded with probability $1/n$; i) along the straight path Γ spanned by El Faro while drifting at an estimated approximate average speed of 2.5 m/s over a time interval of 10 minutes (blue), ii) and also accounting for the vessel size ($241 \times 30 \text{ m}^2$) (black), and over the strip area ($1500 \times 30 \text{ m}^2$) spanned by the vessel in a 10-minute interval (red). Confidence bands are also shown (light dashes). Horizontal line denotes the threshold $1.6H_s \approx 14 \text{ m}$, which is exceeded with probability $3 \cdot 10^{-4}$, $1/400$ and $1/100$ for the three cases shown.

The exceedance probability $P_e(h)$ is formulated as follows. Consider a random wave field whose surface elevation at a given point (x, y) in a fixed frame at time t is $\eta(x, y, t)$. Consider a vessel of area A that navigates through the wave field at a constant speed V along a straight path at an angle β with respect to the x axis. Define also (x_e, y_e) as a cartesian frame moving with the ship. Then, the line trajectories of any point (x_e, y_e) of the vessel in the fixed frame are given by

$$x = x_e + V \cos(\beta)t, \quad y = y_e + V \sin(\beta)t, \tag{8}$$

where for simplicity we assume that at time $t = 0$ the center of gravity of the vessel is at the origin of the fixed frame.

The surface height $\eta_c(t)$ encountered by the moving vessel, or equivalently the surface fluctuations measured by a wave probe installed on the ship, is

$$\eta_c(x_e, y_e, t) = \eta(x_e + V \cos(\beta)t, y_e + V \sin(\beta)t, t), \tag{9}$$

If η is a Gaussian wave field homogeneous in space and stationary in time, then so is η_c with respect to the moving frame (x_e, y_e, t) . The associated space-time covariance is given by

$$\begin{aligned} \Psi(X, Y, T) &= \overline{\eta_c(x_e, y_e, t)\eta_c(x_e + X, y_e + Y, t + T)} \\ &= \int S(f, \theta) \cos(k_x X + k_y Y - 2\pi f_e T) df d\theta, \end{aligned} \tag{10}$$

where $k_x = k \cos(\theta)$, $k_y = k \sin(\theta)$ and k is the wavenumber associated with the frequency f by way of the wave dispersion relation. As a result of the Doppler effect, the encountered, or apparent frequency is given by⁵⁷⁻⁶⁰

$$f_e = f - kV \cos(\theta - \beta)/(2\pi), \tag{11}$$

and $S(f, \theta)$ is the directional wave spectrum of the sea state. Note that when the vessel moves faster than waves coming from a direction θ , the apparent frequency $f_e < 0$ and for an observer on the ship waves appear to move away from him/her. In this case, the direction of those waves should be reversed⁵⁷, i.e. $\theta = \theta + \pi$, and f_e set as positive.

The spectral moments $m_{ijk}^{(e)}$ of the encountered random field readily follow from the coefficients of the Taylor series expansion of $\Psi(X, Y, T)$ around $(X = 0, Y = 0, T = 0)$. In particular,

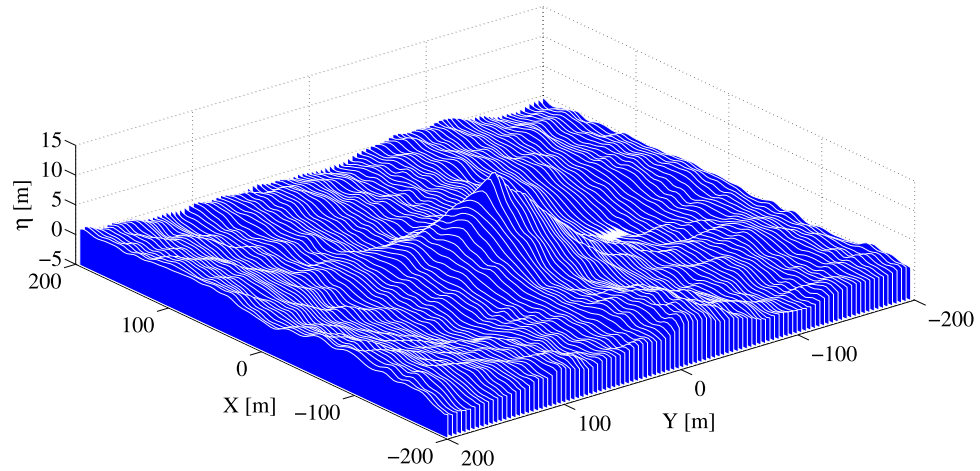


Figure 11. HOS simulations: expected spatial shape of a rogue wave whose crest height is $>1.6H_s \approx 14$ m.

$$m_{ijk}^{(e)} = \frac{\partial^{i+j+k}\Psi}{\partial X^i \partial Y^j \partial T^k} \Big|_{X=Y=T=0} = \int S(f, \theta) k_x^i k_y^j k_z^k df d\theta. \quad (12)$$

The nonlinear space-time statistics can then easily be processed by using the encountered spectral moments $m_{ijk}^{(e)}$ using the FST model^{3,5}, which is based on Eq. (2) as described above. Note that for generic navigation routes the encountered wave field η_c is a non-stationary random process of time. Thus, the associated spectral moments will vary in time. The space-time statistics can be still computed by first approximating the route by a polygonal made of piecewise straight segments along which the random process η_c is assumed stationary.

Figure 10 illustrates the HOS and theoretical predictions for the normalized nonlinear threshold h_n/H_s exceeded with probability $1/n$, where n is the number of waves. In particular, consider an observer on the vessel moving along the straight path Γ spanned by El Faro drifting against the dominant sea direction over a time interval of 10 minutes. In space-time the observer spans the solid red line shown in Fig. 8. In this case, he has a probability $P_e \sim 3 \cdot 10^{-4}$ to encounter a wave whose crest height exceeds the threshold $1.6H_s \approx 14$ m (blue lines), and the expected spatial shape is shown in Fig. 11. If we also account for the vessel size (base area $A = 241 \times 30 \text{ m}^2$), in space-time El Faro spans the volume of the slanted parallelepiped V_a shown in Fig. 8. In this case, the exceedance probability $P_e(V_a)$ further increases to $1/400$ (black lines in Fig. 10). Note that if the vessel would be anchored at a location for the same duration, in spacetime it would span instead the volume of the vertical parallelepiped V_c shown in the same Figure. Note that the two parallelepipeds cover the same space-time volume $A \times D$, with the base area A and height $D = 10 \text{ min}$. For the case of the anchored vessel, the associated exceedance probability $P_e(V_c)$ is roughly the same as $P_e(V_a)$ since El Faro was drifting at a slow speed. Larger drift speeds yield larger $P_e(V_a)$ since the vessel encounters waves more frequently than if it was anchored, because of the Doppler effect^{58,59}. Moreover, the drifting vessel covers the strip area ($1500 \times 30 \text{ m}^2$) in the 10-minute interval and the associated space-time volume is that of the parallelepiped V_b shown in Fig. 8, which has a larger volume than that of V_a . As a result, the occurrence frequency $P_e(V_b)$ of a rogue wave associated with V_b is larger and it increases to $\sim 1/100$ (see red lines in Fig. 10). However, El Faro does not visit the entire volume V_b , but it only spans the smaller volume V_a . Thus, the conditional probability $P_e(V_a|V_b)$ that the drifting El Faro encounters a rogue wave given that a rogue wave occurred over the larger spacetime volume V_b is $P_e(V_a)/P_e(V_b) \sim 1/4$. Furthermore, a fixed observer has a much lower probability $P_e \sim 10^{-6}$ to pick randomly from a time series extracted at a point a wave whose crest height exceeds $1.6H_s$ (see Fig. 6, TF model, black solid line). Finally, we observed that the exceedance probability $P_e(V_a)$ for the drifting El Faro does not scale linearly with time because of nonlinearities that reduce the natural dispersion of waves. Indeed, assuming that El Faro drifts over a time interval 5 times longer (50 minutes), $P_e(V_a)$ just increases roughly by 3 times, $\sim 1/130$.

Discussions

Our present studies open a new research direction on the prediction of rogue waves during hurricanes using the WW3 wave model combined with HOS simulations and the new stochastic FST model⁵ for the prediction of space-time wave extremes^{3,4}. Any wave growth associated with wind stresses, dissipation due to wave breaking and exact nonlinear resonant four-wave interactions is accounted for in the WW3 model. It is the wave growth associated with quasi-resonant and bound harmonics nonlinearities that is not modeled. Such nonlinear effects can locally increase the wave amplitude over the expected values of the WW3 simulations. In our analysis, quasi-resonant and bound nonlinearities are modeled by way of a HOS wave solver that simulated the sea state around the time and location of the accident. The HOS simulations provided an estimate of the most likely rogue wave amplitude over a given area and time interval indicating that bound nonlinearities are dominant, in agreement with recent rogue-wave studies⁷. Our analysis also suggests new studies on the possible effects of factors such as wind gustiness²⁷ and wave breaking^{28,29} on generating rogue waves and associated statistics.

Methods

Wave parameters. The significant wave height H_s is defined as the mean value $H_{1/3}$ of the highest one-third of wave heights. It can be estimated either from a zero-crossing analysis or more easily but approximately from the wave omnidirectional spectrum $S_o(f) = \int_0^{2\pi} S(f, \theta) d\theta$ as $H_s \approx 4\sigma$, where $\sigma = \sqrt{m_0}$ is the standard deviation of surface elevations, $m_j = \int S_o(f) f^j df$ are spectral moments. Further, $S(f, \theta)$ is the directional wave spectrum with θ as the direction of waves at frequency f , and the cyclic frequency is $\omega = 2\pi f$.

The dominant wave period $T_p = 2\pi/\omega_p$ refers to the cyclic frequency ω_p of the spectral peak. The mean zero-crossing wave period T_0 is equal to $2\pi/\omega_0$, with $\omega_0 = \sqrt{m_2/m_0}$. The associated wavelength $L_0 = 2\pi/k_0$ follows from the linear dispersion relation $\omega_0 = \sqrt{gk_0 \tanh(k_0 d)}$, with d the water depth. The mean spectral frequency is defined as $\omega_m = m_1/m_0$ ⁸ and the associated mean period T_m is equal to $2\pi/\omega_m$. A characteristic wave steepness is defined as $\mu_m = k_m \sigma$, where k_m is the wavenumber corresponding to the mean spectral frequency ω_m ⁸. The following quantities are also introduced: $q_m = k_m d$, $Q_m = \tanh q_m$, the phase velocity $c_m = \omega_m/k_m$, the group velocity $c_g = c_m [1 + 2q_m/\sinh(2q_m)]/2$.

The spectral bandwidth $\nu = (m_0 m_2 / m_1^2 - 1)^{1/2}$ gives a measure of the frequency spreading. The angular spreading $\sigma_\theta = \sqrt{\int_0^{2\pi} D(\theta) (\theta - \theta_m)^2 d\theta}$, where $D(\theta) = \int_0^\infty S(\omega, \theta) d\omega / \sigma^2$ and $\theta_m = \int_0^{2\pi} D(\theta) \theta d\theta$ is the mean direction. Note that $\omega_0 = \omega_m \sqrt{1 + \nu^2}$.

The wave skewness λ_3 and the excess kurtosis λ_{40} of the zero-mean surface elevation $\eta(t)$ are given by

$$\lambda_3 = \overline{\eta^3} / \sigma^3, \quad \lambda_{40} = \overline{\eta^4} / \sigma^4 - 3. \quad (13)$$

Here, overbars imply statistical averages and σ is the standard deviation of surface wave elevations.

For second-order waves in deep water¹⁰

$$\lambda_3 \approx 3\mu_m (1 - \nu + \nu^2), \quad (14)$$

and the following bounds hold⁶¹

$$3\mu_m (1 - \sqrt{2}\nu + \nu^2) \leq \lambda_3 \leq 3\mu_m. \quad (15)$$

Here, ν is the spectral bandwidth defined above and the characteristic wave steepness $\mu_m = k_m \sigma$, where k_m is the wavenumber corresponding to the mean spectral frequency ω_m ⁸. For narrowband (NB) waves, ν tends to zero and the associated skewness $\lambda_{3,NB} = 3\mu_m$ ⁸⁻¹⁰.

For third-order nonlinear random seas the excess kurtosis

$$\lambda_{40} = \lambda_{40}^d + \lambda_{40}^b \quad (16)$$

comprises a dynamic component λ_{40}^d due to nonlinear quasi-resonant wave-wave interactions^{11, 62} and a Stokes bound harmonic contribution λ_{40}^b ⁶³. In deep water it reduces to the simple form $\lambda_{40,NB}^b = 18\mu_m^2 = 2\lambda_{3,NB}^2$ ^{11, 63, 64} where $\lambda_{3,NB}$ is the skewness of narrowband waves⁸.

As for the dynamic component, Fedele¹⁴ recently revisited Janssen's⁶² weakly nonlinear formulation for λ_{40}^d . In deep water, this is given in terms of a six-fold integral that depends on the Benjamin-Feir index $BFI = \sqrt{2} m_m / \nu$ and the parameter $R = \sigma_0^2 / 2\nu^2$, which is a dimensionless measure of the multidirectionality of dominant waves^{11, 15}. As waves become unidirectional (1D) waves R tends to zero and a random narrowband wave train becomes unstable if $BFI > 1$ ⁶⁵.

The Tayfun-Fedele model. We define $P(\xi)$ as the probability that a wave crest observed at a fixed point of the ocean in time exceeds the threshold ξH_s . For weakly nonlinear nonlinear seas, this probability can be described by the third-order Tayfun-Fedele model⁹,

$$P_{TF}(\xi) = \Pr[h > \xi H_s] = \exp(-8\xi_0^2) [1 + \Lambda \xi_0^2 (4\xi_0^2 - 1)], \quad (17)$$

where ξ_0 follows from the quadratic equation $\xi = \xi_0 + 2\mu\xi_0^2$ ⁸. Here, the Tayfun wave steepness $\mu = \lambda_3/3$ is of $O(\mu_m)$ and it is a measure of second-order bound nonlinearities as it relates to the skewness λ_3 of surface elevations¹⁰. The parameter $\Lambda = \lambda_{40} + 2\lambda_{22} + \lambda_{04}$ is a measure of third-order nonlinearities and is a function of the fourth order cumulants λ_{nm} of the wave surface η and its Hilbert transform $\hat{\eta}$ ⁹. In particular, $\lambda_{22} = \overline{\eta^2 \hat{\eta}^2} / \sigma^4 - 1$ and $\lambda_{04} = \overline{\hat{\eta}^4} / \sigma^4 - 3$. In our studies Λ is approximated solely in terms of the excess kurtosis as $\Lambda_{\text{appr}} = 8\lambda_{40}/3$ by assuming the relations between cumulants⁶⁶ $\lambda_{22} = \lambda_{40}/3$ and $\lambda_{04} = \lambda_{40}$. These, to date, have been proven to hold for linear and second-order narrowband waves only¹². For third-order nonlinear seas, our numerical studies indicate that $\Lambda \approx \Lambda_{\text{appr}}$ within a 3% relative error in agreement with observations^{67, 68}.

For second-order seas, referred to as Tayfun sea states³⁴, $\Lambda = 0$ only and P_{TF} in Eq. (17) yields the Tayfun (T) distribution⁸

$$P_T(\xi) = \exp(-8\xi_0^2). \quad (18)$$

For Gaussian seas, $\mu = 0$ and $\Lambda = 0$ and P_{TF} reduces to the Rayleigh (R) distribution

$$P_R(\xi) = \exp(-8\xi^2). \quad (19)$$

Note that the Tayfun distribution represents an exact result for large second order wave crest heights and it depends solely on the steepness parameter defined as $\mu = \lambda_3/3^{10}$.

The Forristall model. The exceedance probability is given by³⁰

$$P_F(\xi) = \exp(-(\xi/\alpha)^\beta), \quad (20)$$

where $\alpha = 0.3536 + 0.2561S_1 + 0.0800U_r$, $\beta = 2 - 1.7912S_1 - 0.5302U_r + 0.284U_r^2$ for multi-directional (short-crested) seas. Here, $S_1 = 2\pi H_s/(gT_m^2)$ is a characteristic wave steepness and the Ursell number $U_r = H_s/(k_m^2 d^3)$, where k_m is the wavenumber associated with the mean period $T_m = m_0/m_1$ and d is the water depth.

Space-Time Statistical Parameters. For space-time extremes, the coefficients in Eq. (3) are given by^{3,69}

$$\begin{aligned} M_3 &= 2\pi \frac{D}{\bar{T}} \frac{\ell_x}{L_x} \frac{\ell_y}{L_y} \alpha_{xyt}, \\ M_2 &= \sqrt{2\pi} \left(\frac{D}{\bar{T}} \frac{\ell_x}{L_x} \sqrt{1 - \alpha_{xt}^2} + \frac{D}{\bar{T}} \frac{\ell_y}{L_y} \sqrt{1 - \alpha_{yt}^2} + \frac{\ell_x}{L_x} \frac{\ell_y}{L_y} \sqrt{1 - \alpha_{xy}^2} \right), \\ M_1 &= N_D + N_x + N_y, \end{aligned}$$

where

$$N_D = \frac{D}{\bar{T}}, \quad N_x = \frac{\ell_x}{L_x}, \quad N_y = \frac{\ell_y}{L_y}$$

are the average number of waves occurring during the time interval D and along the x and y sides of length ℓ_x and ℓ_y , respectively. They all depend on the mean period \bar{T} , mean wavelengths \bar{L}_x and \bar{L}_y in x and y directions:

$$\bar{T} = 2\pi \sqrt{\frac{m_{000}}{m_{002}}}, \quad \bar{L}_x = 2\pi \sqrt{\frac{m_{000}}{m_{200}}}, \quad \bar{L}_y = 2\pi \sqrt{\frac{m_{000}}{m_{020}}}$$

and

$$\alpha_{xyt} = \sqrt{1 - \alpha_{xt}^2 - \alpha_{yt}^2 - \alpha_{xy}^2 + 2\alpha_{xt}\alpha_{yt}\alpha_{xy}}.$$

Here,

$$m_{ijk} = \iint k_x^i k_y^j f^k S(f, \theta) df d\theta$$

are the moments of the directional spectrum $S(f, \theta)$ and

$$\alpha_{xt} = \frac{m_{101}}{\sqrt{m_{200}m_{002}}}, \quad \alpha_{yt} = \frac{m_{011}}{\sqrt{m_{020}m_{002}}}, \quad \alpha_{xy} = \frac{m_{110}}{\sqrt{m_{200}m_{020}}}.$$

The Higher Order Spectral (HOS) method. The HOS, developed independently by Dommermuth & Yue²⁵ and West *et al.*²⁶ is a numerical pseudo-spectral method, based on a perturbation expansion of the wave potential function up to a prescribed order of nonlinearities M in terms of a small parameter, the characteristic wave steepness. The method solves for nonlinear wave-wave interactions up to the specified order M of a number N of free waves (Fourier modes). The associated boundary value problem is solved by way of a pseudo-spectral technique, ensuring a computational cost which scales linearly with $M^2 N \log(N)$ ^{70,71}. As a result, high computational efficiency is guaranteed for simulations over large spatial domains. In our study we used the West formulation²⁶, which accounts for all the nonlinear terms at a given order of the perturbation expansion. The details of the specific algorithm are given in Fucile⁷⁰ and Fedele *et al.*². The wave field is resolved using 1024×1024 Fourier modes on a spatial area of $4000 \text{ m} \times 4000 \text{ m}$. Initial conditions for the wave potential and surface elevation are specified from the directional spectrum as an output of WAVEWATCH III⁷².

Data Availability. All the publicly available data and information about the El Faro accident are posted on the National Transportation Safety Board (NTSB) website¹.

References

- National transportation safety board, sinking of the freight vessel el faro, https://www.nts.gov/investigations/Pages/2015_elfaro_jax.aspx (2016).
- Fedele, F., Lugni, C., Fucile, F. & Campana, E. F. On the prediction of rogue waves during hurricane joaquin NTSB - DCA16MM001, <http://dms.nts.gov/public/58000-58499/58116/598564.pdf> (2016).
- Fedele, F. Space-time extremes in short-crested storm seas. *Journal of Physical Oceanography* **42**, 1601–1615, doi:<https://doi.org/10.1175/JPO-D-11-0179.1> (2012).

4. Fedele, F. *et al.* Space–time measurements of oceanic sea states. *Ocean Modelling* **70**, 103–115 (2013).
5. Fedele, F. On oceanic rogue waves. *arXiv preprint arXiv:1501.03370* (2015).
6. Richards, M. The meteorology group factual report for the el faro accident NTSB - DCA16MM001, <http://dms.nts.gov/pubdms/search/document.cfm?docID=447450&docketID=58116&mkey=92109> (2016).
7. Fedele, F., Brennan, J., Ponce de León, S., Dudley, J. & Dias, F. Real world ocean rogue waves explained without the modulational instability. *Scientific Reports* **6**, 27715 EP – (2016).
8. Tayfun, M. A. Narrow-band nonlinear sea waves. *Journal of Geophysical Research: Oceans* **85**, 1548–1552, doi:<https://doi.org/10.1029/JC085iC03p01548> (1980).
9. Tayfun, M. A. & Fedele, F. Wave-height distributions and nonlinear effects. *Ocean Engineering* **34**, 1631–1649, doi:<https://doi.org/10.1016/j.oceaneng.2006.11.006> (2007).
10. Fedele, F. & Tayfun, M. A. On nonlinear wave groups and crest statistics. *J. Fluid Mech* **620**, 221–239 (2009).
11. Janssen, P. A. E. M. & Bidlot, J. R. On the extension of the freak wave warning system and its verification. Tech. Memo 588, ECMWF (2009).
12. Tayfun, M. A. & Lo, J. Nonlinear effects on wave envelope and phase. *J. Waterway, Port, Coastal and Ocean Eng.* **116**, 79–100 (1990).
13. Fedele, F. Rogue waves in oceanic turbulence. *Physica D* **237**, 2127–2131 (2008).
14. Fedele, F. On the kurtosis of ocean waves in deep water. *Journal of Fluid Mechanics* **782**, 25–36 (2015).
15. Mori, N., Onorato, M. & Janssen, P. A. E. M. On the estimation of the kurtosis in directional sea states for freak wave forecasting. *Journal of Physical Oceanography* **41**, 1484–1497, doi:<https://doi.org/10.1175/2011JPO4542.1> (2011).
16. Onorato, M. *et al.* Statistical properties of mechanically generated surface gravity waves: a laboratory experiment in a three-dimensional wave basin. *Journal of Fluid Mechanics* **627**, 235–257, doi:<https://doi.org/10.1017/S002211200900603X> (2009).
17. Waseda, T., Kinoshita, T. & Tamura, H. Evolution of a random directional wave and freak wave occurrence. *Journal of Physical Oceanography* **39**, 621–639, doi:<https://doi.org/10.1175/2008JPO4031.1> (2009).
18. Toffoli, A. *et al.* Evolution of weakly nonlinear random directional waves: laboratory experiments and numerical simulations. *Journal of Fluid Mechanics* **664**, 313–336, doi:<https://doi.org/10.1017/S002211201000385X> (2010).
19. Annenkov, S. Y. & Shrira, V. I. Large-time evolution of statistical moments of wind–wave fields. *Journal of Fluid Mechanics* **726**, 517–546, doi:<https://doi.org/10.1017/jfm.2013.243> (2013).
20. Annenkov, S. Y. & Shrira, V. I. Evaluation of skewness and kurtosis of wind waves parameterized by JONSWAP spectra. *Journal of Physical Oceanography* **44**, 1582–1594, doi:<https://doi.org/10.1175/JPO-D-13-0218.1> (2014).
21. Fedele, F. On certain properties of the compact zakharov equation. *Journal of Fluid Mechanics* **748**, 692–711, doi:<https://doi.org/10.1017/jfm.2014.192> (2014).
22. Tayfun, M. A. Distributions of envelope and phase in wind waves. *Journal of Physical Oceanography* **38**, 2784–2800, doi:<https://doi.org/10.1175/2008JPO4008.1> (2008).
23. Christou, M. & Ewans, K. Field measurements of rogue water waves. *Journal of Physical Oceanography* **44**, 2317–2335, doi:<https://doi.org/10.1175/JPO-D-13-0199.1> (2014).
24. Nārhi, M. *et al.* Real-time measurements of spontaneous breathers and rogue wave events in optical fibre modulation instability. *Nature Communications* **7**, 1–9, doi:<https://doi.org/10.1038/ncomms13675> (2016).
25. Dommermuth, D. G. & Yue, D. K. P. A high-order spectral method for the study of nonlinear gravity waves. *Journal of Fluid Mechanics* **184**, 267–288, doi:<https://doi.org/10.1017/S002211208700288X> (1987).
26. West, B., Brueckner, K., Janda, R., Milder, M. & Milton, R. A new numerical method for surface hydrodynamics. *Journal of Geophysical Research* **92**, 11803–11824, doi:[https://doi.org/10.1016/S0169-5983\(00\)00011-3](https://doi.org/10.1016/S0169-5983(00)00011-3) (1987).
27. Pleskachevsky, A. L., Lehner, S. & Rosenthal, W. Storm observations by remote sensing and influences of gustiness on ocean waves and on generation of rogue waves. *Ocean Dynamics* **62**, 1335–1351, doi:<https://doi.org/10.1007/s10236-012-0567-z> (2012).
28. Barthelemy, X. *et al.* On the local properties of highly nonlinear unsteady gravity water waves. part 2. dynamics and onset of breaking. *Journal of Fluid Mechanics (submitted)* <http://arxiv.org/abs/1508.06002> (2015).
29. Saket, A., Peirson, W. L., Banner, M. L., Barthelemy, X. & Allis, M. J. On the threshold for wave breaking of two-dimensional deep water wave groups in the absence and presence of wind. *Journal of Fluid Mechanics* **811**, 642–658, doi:<https://doi.org/10.1017/jfm.2016.776> (2017).
30. Forristall, G. Z. Wave crest distributions: Observations and second-order theory. *Journal of Physical Oceanography* **30**, 1931–1943, doi:<https://doi.org/10.1175/1520-0485> (2000).
31. Donelan, M. A. & Magnusson, A.-K. The making of the andrea wave and other rogues. *Scientific Reports* **7**, 44124 (2017).
32. Dysthe, K. B., Krogstad, H. E. & Muller, P. Oceanic rogue waves. *Annual Review of Fluid Mechanics* **40**, 287–310 (2008).
33. Flanagan, J. *et al.* ADCP measurements of extreme water waves off the west coast of Ireland. In *The Proceedings of the 26th (2016) International Offshore and Polar Engineering, Rhodes, Greece, June 26 - July 2, 2016* (International Society of Offshore and Polar Engineers, 2016).
34. Trulsen, K., Nieto Borge, J. C., Gramstad, O., Aouf, L. & Lefèvre, J.-M. Crossing sea state and rogue wave probability during the Prestige accident. *Journal of Geophysical Research: Oceans* **120**, doi:<https://doi.org/10.1002/2015JC011161> (2015).
35. Boccotti, P. *Wave Mechanics for Ocean Engineering* (Elsevier Sciences, Oxford, 2000).
36. Gemmrich, J. & Thomson, J. Observations of the shape and group dynamics of rogue waves. *Geophysical Research Letters* **44**, 1823–1830, doi:<https://doi.org/10.1002/2016GL072398>. 2016GL072398 (2017).
37. Fedele, F. Are rogue waves really unexpected? *Journal of Physical Oceanography* **46**, 1495–1508, doi:<https://doi.org/10.1175/JPO-D-15-0137.1> (2016).
38. Birkholz, S., Brée, C., Veselić, I., Demircan, A. & Steinmeyer, G. Ocean rogue waves and their phase space dynamics in the limit of a linear interference model. *Scientific reports* **6** (2016).
39. Bitner-Gregersen, E. M. & Toffoli, A. Occurrence of rogue sea states and consequences for marine structures. *Ocean Dynamics* **64**, 1457–1468, doi:<https://doi.org/10.1007/s10236-014-0753-2> (2014).
40. Dudley, J. M., Sarano, V. & Dias, F. On hokusai's great wave off kanagawa: localization, linearity and a rogue wave in sub-antarctic waters. *Notes Rec. R. Soc.* **67**, 159–164 (2013).
41. Gemmrich, J. & Garrett, C. Unexpected waves. *Journal of Physical Oceanography* **38**, 2330–2336 (2008).
42. Mathis, A. *et al.* Caustics and rogue waves in an optical sea. *Scientific Reports* **5**, doi:<https://doi.org/10.1038/srep12822> (2015).
43. Walker, D., Taylor, P. & Taylor, R. E. The shape of large surface waves on the open sea and the Draupner new year wave. *Applied Ocean Research* **26**, 73–83, doi:<https://doi.org/10.1016/j.apor.2005.02.001> (2004).
44. Fedele, F., Chandre, C. & Farazmand, M. Kinematics of fluid particles on the sea surface: Hamiltonian theory. *Journal of Fluid Mechanics* **801**, 260–288, doi:<https://doi.org/10.1017/jfm.2016.453> (2016).
45. Fedele, F. Geometric phases of water waves. *EPL (Europhysics Letters)* **107**, 69001 (2014).
46. Adcock, T., Taylor, P., Yan, S., Ma, Q. & Janssen, P. Did the Draupner wave occur in a crossing sea? *Proceedings of the Royal Society A: Mathematical, Physical and Engineering Science* rspa20110049 (2011).
47. Cavaleri, L. *et al.* The draupner wave: a fresh look and the emerging view. *Journal of Geophysical Research: Oceans* **121**, 6061–6075 (2016).
48. Longuet-Higgins, M. S. & Stewart, R. W. Radiation stresses in water waves: a physical discussion, with applications. *Deep-Sea Research II*, 529–562 (1964).
49. Adler, R. J. *The geometry of random fields*, vol. 62 (Siam, 1981).

50. Adler, R. J. & Taylor, J. E. *Random fields and geometry*, vol. 115 (Springer Monographs in Mathematics, 2009).
51. Adler, R. J. On excursion sets, tube formulas and maxima of random fields. *Annals of Applied Probability* 1–74 (2000).
52. Barbariol, F. et al. Numerical modeling of space-time wave extremes using wavewatch iii. *Ocean Dynamics* 1–15 (2017).
53. Piterbarg, V. I. *Asymptotic methods in the theory of Gaussian processes and fields*, vol. 148 (AMS ser. Translations of Mathematical Monographs, 1995).
54. Socquet-Juglard, H., Dysthe, K. B., Trulsen, K., Krogstad, H. E. & Liu, J. Probability distributions of surface gravity waves during spectral changes. *Journal of Fluid Mechanics* 542, 195–216, doi:<https://doi.org/10.1017/S0022112005006312> (2005).
55. Forristall, G. Z. Maximum crest heights under a model tlp deck. In *ASME 2011 30th International Conference on Ocean, Offshore and Arctic Engineering*, 571–577 (American Society of Mechanical Engineers, 2011).
56. Forristall, G. Z. Maximum crest heights over an area: laboratory measurements compared to theory. In *ASME 2015 34th International Conference on Ocean, Offshore and Arctic Engineering*, OMAE2015–41061 (American Society of Mechanical Engineers, 2015).
57. St. Denis, M. & Pierson, W. On the motions of ships in confused seas. *Transactions, The Society of Naval Architects and Marine Engineers* 61, 280–357 (1953).
58. Lindgren, G., Rychlik, I. & Prevosto, M. Stochastic doppler shift and encountered wave period distributions in gaussian waves. *Ocean Engineering* 26, 507–518, doi:[https://doi.org/10.1016/S0029-8018\(98\)00015-8](https://doi.org/10.1016/S0029-8018(98)00015-8) (1999).
59. Podgorski, K., Rychlik, I. & Machado, U. E. Exact distributions for apparent waves in irregular seas. *Ocean Engineering* 27, 979–1016 (2000).
60. Soares, G. C., Fonseca, N. & Pascoal, R. Abnormal wave-induced load effects in ship structures. *Journal of ship research* 52, 30–44 (2008).
61. Tayfun, M. A. Statistics of nonlinear wave crests and groups. *Ocean Engineering* 33, 1589–1622, doi:<https://doi.org/10.1016/j.oceaneng.2005.10.007> (2006).
62. Janssen, P. A. E. M. Nonlinear four-wave interactions and freak waves. *Journal of Physical Oceanography* 33, 863–884 (2003).
63. Janssen, P. A. E. M. On some consequences of the canonical transformation in the hamiltonian theory of water waves. *Journal of Fluid Mechanics* 637, 1–44, doi:<https://doi.org/10.1017/S0022112009008131> (2009).
64. Janssen, P. A. E. M. On a random time series analysis valid for arbitrary spectral shape. *Journal of Fluid Mechanics* 759, 236–256, doi:<https://doi.org/10.1017/jfm.2014.565> (2014).
65. Alber, I. E. The effects of randomness on the stability of two-dimensional surface wavetrains. *Proceedings of the Royal Society of London A: Mathematical, Physical and Engineering Sciences* 363, 525–546 (1978).
66. Mori, N. & Janssen, P. A. E. M. On kurtosis and occurrence probability of freak waves. *Journal of Physical Oceanography* 36, 1471–1483, doi:<https://doi.org/10.1175/JPO2922.1> (2006).
67. Fedele, F., Cherneva, Z., Tayfun, M. A. & Soares, C. G. Nonlinear Schrödinger invariants and wave statistics. *Physics of Fluids* 22, 036601, doi:<https://doi.org/10.1063/1.3325585> (2010).
68. Tayfun, M. A. & Fedele, F. Expected shape of extreme waves in storm seas. In *ASME 2007 26th International Conference on Offshore Mechanics and Arctic Engineering*, OMAE2007–29073 (American Society of Mechanical Engineers, 2007).
69. Baxevani, A. & Rychlik, I. Maxima for gaussian seas. *Ocean Engineering* 33, 895–911, doi:<https://doi.org/10.1016/j.oceaneng.2005.06.006> (2006).
70. Fucile, F. *Deterministic sea wave and ship motion forecasting: from remote wave sensing to prediction error assessment* (PhD Thesis, Univ. of Trieste, 2017).
71. Schäffer, H. Comparison of dirichlet–neumann operator expansions for nonlinear surface gravity waves. *Coastal Engineering* 55, 288–294, doi:<https://doi.org/10.1016/j.coastaleng.2007.11.002> (2008).
72. Tolman, H. & Group, D. User manual and system documentation of WAVEWATCH III version 4.18. Tech. Rep. Tech. Note 316, NOAA/NWS/NCEP/MMAB (2014).

Acknowledgements

This manuscript is based on a study on the prediction of rogue waves during Hurricane Joaquin provided as a supplement to the National Transportation Safety Board (NTSB) to assist them in their investigation of the sinking of the Merchant Vessel El Faro, which occurred east of the Bahamas on October 1, 2015. The authors thank Emilio F. Campana for his support and incisive intellectual discussions and Fabio Fucile for helping with the HOS simulations. C. Lugni was supported by the Research Council of Norway through the Centres of Excellence funding scheme AMOS, project number 223254 and by the Flagship Project RITMARE - The Italian Research for the Sea - coordinated by the Italian National Research Council.

Author Contributions

The concept and design was provided by F. Fedele, who coordinated the scientific effort together with C. Lugni. C. Lugni performed numerical simulations and developed specific codes for the analysis. The wave statistical analysis was performed by F. Fedele together with C. Lugni. The overall supervision was provided by F. Fedele; A. Chawla performed the WAVEWATCH simulations and made ongoing incisive intellectual contributions. All authors participated in the analysis and interpretation of results and the writing of the manuscript.

Additional Information

Competing Interests: The authors declare that they have no competing interests.

Publisher's note: Springer Nature remains neutral with regard to jurisdictional claims in published maps and institutional affiliations.



Open Access This article is licensed under a Creative Commons Attribution 4.0 International License, which permits use, sharing, adaptation, distribution and reproduction in any medium or format, as long as you give appropriate credit to the original author(s) and the source, provide a link to the Creative Commons license, and indicate if changes were made. The images or other third party material in this article are included in the article's Creative Commons license, unless indicated otherwise in a credit line to the material. If material is not included in the article's Creative Commons license and your intended use is not permitted by statutory regulation or exceeds the permitted use, you will need to obtain permission directly from the copyright holder. To view a copy of this license, visit <http://creativecommons.org/licenses/by/4.0/>.